Delft University of Technology

New insights into hydrogen trapping and embrittlement in high strength aluminum alloys

Safyari, Mahdieh; Khossossi, Nabil; Meisel, Thomas; Dey, Poulumi; Prohaska, Thomas; Moshtaghi, Masoud

Important note
To cite this publication, please use the final published version (if applicable).
Please check the document version above.

New insights into hydrogen trapping and embrittlement in high strength aluminum alloys

Mahdieh Safyari [a,b,c,*], Nabil Khossossi [d], Thomas Meisel [a], Poulumi Dey [d], Thomas Prohaska [a], Masoud Moshtaghi [a,**]

[a] *Chair of General and Analytical Chemistry, Montanuniversität Leoben, Franz Josef-Straße 18, 8700 Leoben, Austria*
[b] *Institute for Materials Research, Tohoku University, 2-1-1 Katahira, Aoba-ku, Sendai 980-8577, Japan*
[c] *LKR Light Metals Technologies Ranshofen, Austrian Institute of Technology, 5282 Ranshofen, Austria*
[d] *Department of Materials Science and Engineering, Faculty of Mechanical, Maritime and Materials Engineering, Delft University of Technology, Mekelweg 2, 2628 CD, Delft, the Netherlands*

ARTICLE INFO

ABSTRACT

An attractive approach to mitigate hydrogen embrittlement (HE) is to use nano-sized particles to immobilize hydrogen. However, the atomic scale relationship between different particle-matrix characteristics in aluminum alloys and the susceptibility to HE is unknown. In this study, the effects of interactions between various interfaces and hydrogen in aluminum alloys are investigated using a comprehensive multiscale experimental and simulation-based approach that includes atomic-scale observations, simulation and advanced hydrogen mapping techniques. Depending on the nature of interfaces, e.g., coherency, size, and crystal structure, some are useful for mitigating HE, others provide hydrogen to sensitive sites, and some act as crack initiation sites.

1. Introduction

The susceptibility of high-strength aluminum alloys to environmentally assisted hydrogen embrittlement (HE) has been until now the subject of significant attention due to their extensive applications in commercial aircraft [1,2]. Nowadays, with the approach of energy transition in aerospace industries to green energies, there are extensive demands for designing a new series of high-strength light alloys that can withstand possible environmental HE. A new generation of zero-emission aircraft is currently being developed by top-tier aircraft manufacturers. The state-of-the-art design of zero-emission aircrafts includes hydrogen combustion through modified gas turbine engines of the existing commercial aircraft. This design was established based on using liquid hydrogen as a fuel for combustion with oxygen. The hydrogen burning results in the production of a high amount of water vapor, exposing the applied high-strength aluminum alloys to the water vapor for a long time. Under the combined influence of tensile stress and absorption of hydrogen through water vapor, hydrogen is produced by reactions on newly generated surfaces where a part of atomic hydrogen can enter into the aluminum alloy [3]. The atomic hydrogen moves into

the bulk of the alloy and may be trapped at a variety of preferential sites. Despite the high demand for a new series of aluminum alloys for the application in zero-emission aircraft, the fundamental understanding of the role of micro/nanostructure variables on microstructure-based material design of high-strength aluminum alloys for application in zero-emission aircraft is not clarified yet.

Some efforts have been made to enhance the HE resistance via chemical composition optimization [4] or alloy processing such as aging treatment, solution treatment [2], pre-deformation [5], a combination of pre-deformation and heat treatment [6], and surface treatment [7]. However, these results lead to sacrificing mechanical properties in preference to HE resistance. Homogenization is a high-temperature heat treatment carried out after casting and consists of three distinct steps: heat-up, soak, and cool-down. This procedure is performed at 450–500 °C on various alloy compositions in order to decrease the micro-scale solute segregations that appeared through casting. Furthermore, some nanoparticles appear during homogenization in Zr, Sc, Cr, or Mn-containing alloys. The nanoparticles have a considerable effect on inhibiting grain growth and reducing recrystallization during the next high-temperature treatments [8]. Thus, homogenization

---

considerably influences the micro/nanostructure variables and corresponding mechanical properties of 7xxx series aluminum alloys.

Several studies have been conducted about the HE behavior of aluminum alloys. Some studies have been conducted to examine the effect of Zr alloying on the HE behavior of high-strength aluminum alloys. Some of these reports showed that Zr dramatically increases the HE sensitivity of high-strength aluminum alloys [9,10] while Zhao et al. [11] reported that the addition of Zr to high-strength aluminum alloys is beneficial to reduce HE sensitivity. However, it is still not clear when Zr addition exacerbates HE and when suppresses it. This is due to the lack of investigations on the characteristics of the Zr-containing particles in previous studies. Thus, the role of nanoparticle engineering in Al alloys for hydrogen storage was not understood yet. Understanding the effect of these nanoparticles in suppressing or exacerbating environmentally induced hydrogen embrittlement will help to pave the way for the development of a high-strength aluminum alloy that resists hydrogen embrittlement for hydrogen storage in hydrogen-powered aircraft.

Robson [12] indicated that the shape, size, and number density of nanoparticles are influenced by homogenization time and temperature. Further, Liu et al. [13] showed the change in the fracture toughness of an aluminum alloy by altering the size, volume fraction, and characteristics of nanoparticles. Wouters et al. [14] reported a decrease in the ductility of 2024 aluminum alloy as a result of increasing the size of nanoparticles via increasing homogenization temperature. On the other hand, several studies have reported that altering the size, shape and coherency of the particles can significantly change the corrosion rate [15] or the sensitivity of different alloys to HE [16–18]. However, the underlying mechanism is not yet well understood. Therefore, a deeper understanding of hydrogen/ particle interactions needs a detailed investigation of the hydrogen trapping at the second phase particles and the related mechanism.

Several reports suggested that the particle shape and/or coherency have determinant effects on the HE behavior. For instance, sphere-like MnS acts as a hydrogen trap and mitigates HE [19,20] while the plate-like MnS inclusions are mainly hydrogen-assisted crack initiation sites. The misfit strain and the elastic modulus of carbides/Fe interfaces have been reported to be key factors determining the hydrogen trapping capacity of the carbides [16,17,21–23]. Motivated by this context, in the present study, the possible mechanisms of the hydrogen/nanoparticles interactions in a 7xxx aluminum alloy are investigated. Different nanoparticle sizes and number densities are produced during homogenization at different temperatures. Thermal desorption spectroscopy (TDS) is employed to investigate the mechanism of hydrogen distribution at the trap sites including the nanoparticles. Thus, the main parameters which influence the hydrogen trapping at the nanoparticles can be elucidated. Furthermore, in addition to the effects of nanoparticles on HE, their effect on the micro/nanostructure variables and hydrogen properties are also discussed in detail to achieve both optimum strength and HE resistance.

2. Methods

2.1. Materials

Overall chemical compositions of samples were determined using the X-ray fluorescence (XRF) technique, and that was Al-8.46Zn- 2.30Mg- 2.62Cu- 0.14Zr (%wt). The molten alloy was poured into a mold with 60 mm thickness. Then some specimens were cut from the center of the castings. Isothermal homogenization treatments were conducted in a salt bath at different temperatures of 350, 410, 490, and 550 °C for 48 h. Following the homogenization treatments, all the specimens were quenched in cold water. The specimens were subjected to hot rolling at a reduction rate of 80% at 410 °C to a final thickness of 1.25 mm. The hot-rolled sheets were solution heat-treated at 480 °C for 1 h in an argon atmosphere followed by ice water quenching and aging at room temperature for 48 h and then at 120 °C for 24 h. Fig. 1 represents a schematic diagram of the processing schedule of the specimens for the current study.

2.2. High-resolution EBSD

A Hitachi 5000 SEM equipped with an EBSD detector was used. The specimens were prepared with electropolishing followed by flat ion milling in 6 kV, and tilting of 50 ° for 20 min. The tests were performed with a scanning step size of 0.5 μm with a beam voltage of 20 kV to observe the recrystallized structures of the specimens which were polished along the rolling direction beforehand.

2.3. STEM characterizations

The microstructures of the specimens were observed using an atomic resolution electron microscope (JEOL-JEM-ARM200F) which is equipped with spherical aberration correctors to perform typical HAADF-STEM and bright field TEM imaging. For this, the specimens were first mechanically ground and then electro-polished at 15–20 V and − 25 °C using the twin jet polishing method and a solution (20% HNO_3 + 80% Methanol) as an electrolyte. ImageJ was used to calculate the volume fraction of spheroidal nanoparticles in STEM images. Images were converted to black and white mode by adding a brightness threshold, and then the area fraction of secondary phases was calculated [24]. To make sure about the accuracy of the ImageJ analysis, we compared the results once with the conventional TEM method which were obtained from the averaged precipitate volume and the precipitate number density measured by TEM [25].

2.4. Atom probe tomography

APT was performed using a Cameca-LEAP-4000X-HR with a reflection detector system with 37% detection efficiency. The samples were prepared via focused ion beam (FIB) lift-out with a 30 kV Ga^+ beam. The
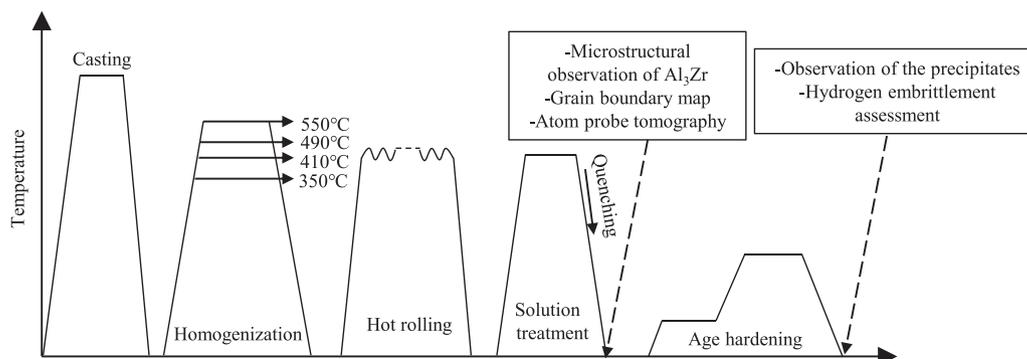

Fig. 1. Schematic diagram of processing schedule of the specimens.

APT was conducted by high-voltage pulses with a repetition frequency of 200 kHz to initiate field evaporation with the specimen bias voltage adjusted to obtain the average detection rate of 2 kHz.

2.5. In-situ tensile tests

Mechanical properties tests were performed on the samples by a slow strain rate tensile testing machine at the initial strain rate of 1.67×10^{-7} s^{-1}. The gauge length, width, and thickness of the specimens were 12 mm, 5 mm, and 1 mm, respectively. To investigate the HE resistance, SSRTs were carried out in dry nitrogen gas (DNG) and humid air (HA) with a relative humidity of 1% and 60%, respectively. To quantify the HE susceptibility, the index, I_{HES}, is defined as the HE susceptibility [18].

$$I_{HES} = 1 - \frac{\delta_{HA}}{\delta_{DNG}} \tag{1}$$

where δ is the elongation. The HE sensitivity increases when the index, I_{HES}, varies from 0 to 1.

2.6. Characterization of fractured specimen via SEM, FIB and TEM

The fracture surfaces after tensile testing were characterized via SEM. To be able to correlate the fracture behavior with microstructure, TEM was performed on the rolling direction (RD)-short transverse (ST) of the specimens. The TEM sample preparation was done using FIB. The FIB lift-out technique has been described in detail elsewhere [26].

2.7. In-situ SKPFM experiment procedure

The scanning kelvin probe force microscopy (SKPFM) measurements were performed under DNG at room temperature using Agilent 5500 AFM. The hydrogen was introduced into the as-solution treated specimens via exposure to hot HA (80 ºC, > 90% relative humidity) for 36 h, and then a thin layer of Pd was physically deposited on the surface of the specimens The Pd layer can be used as a perfect layer for detecting the accumulation of hydrogen, because due to the very low chemical potential of hydrogen in Pd, there is a strong driving force for hydrogen to penetrate the Pd layer and change the potential contrast. Therefore, the potential measured by the SKPFM depends on the hydrogen concentration in the Pd layer. The SKPFM contains a probe with a conductive Pt-coated silicon tip. The tip is vibrated over the surface at different frequencies to measure the potential contrast, which provides important information about the different rates of hydrogen desorption from the traps.

2.8. Thermal desorption spectroscopy

To investigate the hydrogen trapping behavior of the specimens, some tensile tests under HA were stopped at the strain of 0.06 before the fracture of the specimens. Then, the parallel length part ($12.0 \times 5.0 \times 1.0$ mm^3) of each specimen was cut immediately and placed in the TDS furnace. The desorption energy (E_d) can be obtained via heating a sample at some different heating rates (Φ) and using the following equation [27]:

$$\frac{d(\ln(\frac{\varphi}{T_m^2}))}{d(\frac{1}{T_m})} = -\frac{E_d}{R} \tag{2}$$

where T_m is the temperature corresponding to the center of the peaks and R is the gas constant. Then E_d of each trap can be obtained by considering the slope between $d(\ln(\frac{\varphi}{T_m^2}))$ as a function of $d(\frac{1}{T_m})$.

2.9. Density functional theory calculations

To evaluate the hydrogen trapping ability on the unstrained and strained considered systems, we performed Density Functional Theory (DFT) framework as part of the Vienna Ab Initio Simulation Package (VASP) [28]. The standard Generalized Gradient Approximation via Perdew Burke Ernzerhof (GGA-PBE) functional [29] was used self-consistently through the theory of the Projector Augmented Wave (PAW) by the plane wave basis set with a 500 eV kinetic-energy cutoff and the electronic self-consistent energy and forces convergence criteria during the geometry relaxations through the conjugate-gradient algorithm were set to 10^{-6} eV and 10^{-3} eV/Å, respectively.

The Monkhorst-Pack method [30] is employed for the k-point grid with an 8×8x8 grid used for Al (Fm$\bar{3}$m) structure and a 12×12×12 grid used for L1$_2$ -Al$_3$Zr (Pm$\bar{3}$m) and D0$_{23}$-Al$_3$Zr (Pm$\bar{3}$m) structures. These geometrical optimizations are performed within a supercell size of 3×3x3. The criterion for identifying the appropriate hydrogen trapping site was estimated based on the solution energy ($E_S = E$ (trap+H) - E (trap) – $1/2E(H_2)$) of a hydrogen atom at the trapping sites. In addition, hydrogen diffusion was investigated based on the Climbing Image Nudged Elastic Band (CI-NEB) approach [31] which needs to input the initial and final positions of hydrogen diffusion and then, generates a number of intermediate configurations by the linear interpolation. Next, the energy barrier corresponding to hydrogen diffusion between the initial and final states (i.e., from the most stable tetrahedral site to the nearest tetrahedral site) is computed by minimizing the energy and atomic forces in all configurations.

3. Results

3.1. Microstructure

Fig. 2a-d show the high-angle annular dark-field scanning transmission electron microscopy (HAADF-STEM) micrographs of the nanoparticles present in different specimens after solution heat treatment. In Fig. 2e, an example of the selected area diffraction (SAD) pattern shows that the HAADF images use (010) superlattice reflection, and the SAD pattern contains a superlattice spot related to the Al$_3$Zr ordering along with the main α-Al reflections. Also, the different homogenization treatment temperature leads tothe preparation of four types of specimens which are hereafter called according to their homogenization temperatures as H350, H410, H490, and H550, respectively. The finer Al$_3$Zr nanoparticles with a higher number density can form by low-temperature homogenization. The size of nanoparticles and also the widths of the particles-free zone were significantly increased by increasing the homogenization temperature. The average diameter of the nanoparticles was statistically measured to be ~12.5 nm, 21.2 nm, 29.3 nm, and 31.5 nm with volume fractions of 4.46%, 4.78%, 5.69%, and 5.94% for H350, H410, H490, and H550 conditions, respectively. Therefore, changing the homogenization temperature has been shown to be an effective approach to control the distribution of fine nanoparticles. HAADF-STEM was used to observe the Al$_3$Zr nanoparticles (Fig. 2f and g). From the inverse fast Fourier transform (IFFT) image of the H410 specimen (Fig. 2h) the mean D-spacing of the (111) plane in the Al$_3$Zr nanoparticles was measured as 2.345 Å, while that of the Al matrix was 2.332 Å, indicating that the Al$_3$Zr particles are fully coherent with the matrix, with a 0.56% lattice mismatch. The fully semi-coherent Al$_3$Zr nanoparticles were observed in the H490 specimen. The IFFT image (Fig. 2j) of (111) reflection indicates that the lattice mismatch of the semi-coherent Al$_3$Zr particles and the Al matrix increased to 1.81% in this specimen. The obtained results appear to be consistent with the studies [32,33] that reported that the critical radius for coherency loss of Al$_3$Zr nanoparticles in the matrix is ~25 nm meaning that the interfaces of Al$_3$Zr nanoparticles with a size smaller than 25 nm are completely coherent with the matrix, whereas the coarser ones loss their coherency as shown in Fig. 2g and j. It is obvious that the particles which form in lower temperatures than 410 °C and higher temperatures than 490 °C are also fully coherent and semi-coherent, respectively.

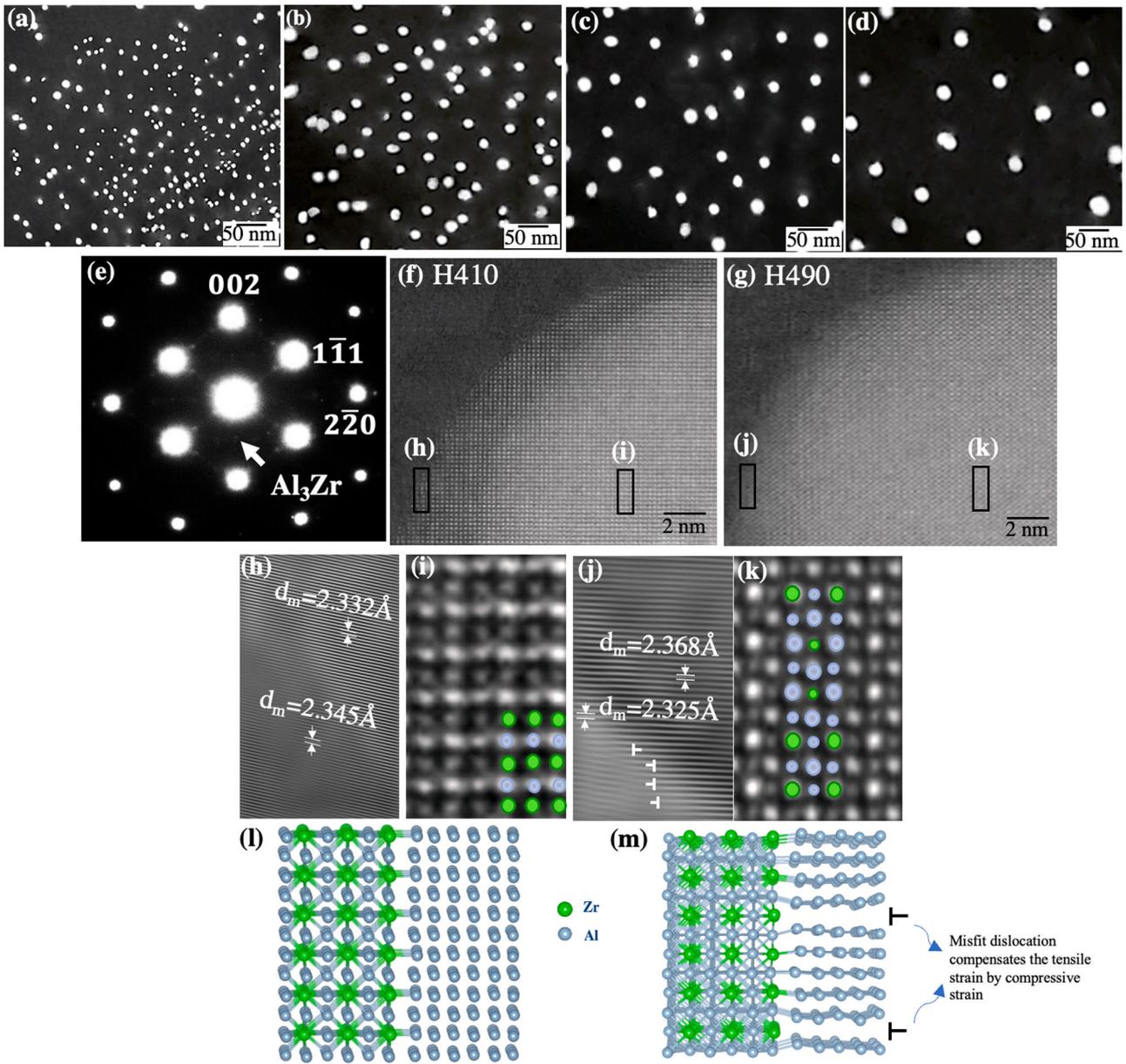Fig. 2j and m also shows that it is more favorable to generate the

Fig. 2. HAADF-STEM micrograph of the (a) H350, (b) H410, (c) H490, (d) H550; (e) an example of the selected area diffraction (SAD) pattern; and HAADF image of Al$_3$Zr dispersoids in (f) H410 and (g) H490 specimens; and (h,j) corresponding inverse fast Fourier transform (IFFT) of the particle/matrix interface in the <001> zone axis of H410, and H490 specimens, respectively. (i,k) Enlarged HAADF-STEM image from the marked region in Fig. (f,g) indicating the atomic structure of the Al$_3$Zr particle. (l,m) The atomistic simulations of the unstrained coherent particle/matrix interface (Fig. l) and the incoherent particle/matrix interface (Fig. m) are reconstructed to observe the interface status. Figs. l and m are rotated compared to the HAADF atomistic observation (Figs. i and k) to be able to see the interfaces.
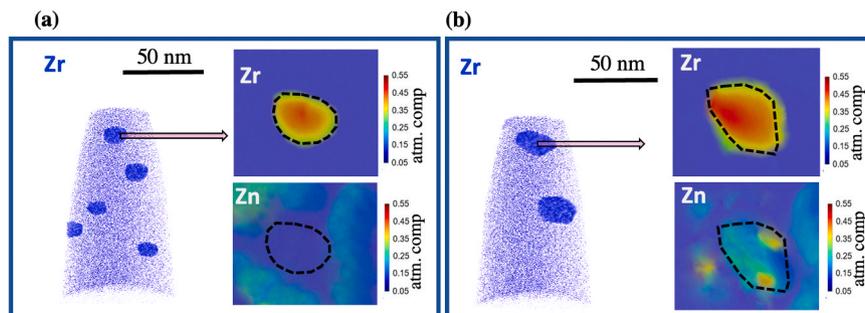

Fig. 3. Individual Zr and Zn maps from atom probe tomography of (a) H350 and (b) H550 specimens.

interfacial misfit dislocations in the nanoparticles/matrix semi-coherent interfaces when the size of nanoparticles is higher than the critical size [34]. The interfacial misfit dislocations shown in Fig. 2j are evidence of the fact that these nanoparticles have lost their coherency during coarsening. In addition, the enlarged image presented in Fig. 2i showed an ordered form of the aluminum face-centered-cubic (fcc) lattice in which Al atoms occupy the face centers and Zr atoms occupy the cell corners. This means that Al₃Zr particles precipitate with an L1₂ crystal structure in the H410 specimen. By increasing the temperature, a transition to the D0₂₃ equilibrium crystal structure occurred (Fig. 2j and k). The D0₂₃ structure with tetragonal symmetry is a crystal system with atoms on the sites of the fcc lattice when $c = 4a$, $z_1 = \frac{3}{8}$, $z_2 = \frac{1}{8}$.

The APT measurements show that the spherical particles are found to be Zr-rich particles (Fig. 3). The results indicate that the L1₂ Al₃Zr nanoparticles are inert with respect to the major alloying elements like Zn (Fig. 3a), however, a slight concentration of Zn was observed in the Al₃Zr particles with D0₂₃ crystal structure (Fig. 3b). The presence of Zn in the semi-coherent particles can affect the interaction of the absorbed atomic H in the microstructure and particles which will be clarified in the next section.

The bright field TEM images of the H410 and H490 specimens in T6 conditions are presented in Fig. 4a, b. The representative SAD pattern (Fig. 4c) shows that the precipitates near the grain boundaries are mainly η'-phases. No significant differences in the shape, size, and distribution of these precipitates were observed around the grain boundaries of the samples with different homogenization temperatures. In addition, Fig. 4d shows that the matrix/Al₃Zr particles in H410 remained coherent after solution treatment and aging, indicating that the next heat treatment does not affect the nature of the interfaces.

An example electron backscattered diffraction (EBSD) inverse pole figure (IPF) map of the rolling direction-long transverse (RD-LT) plane of the samples with different homogenization temperatures ranging from 350 to 550 °C can be seen in Fig. 5a-d. The fraction of recrystallized grains of the specimens in different homogenization conditions increases when the homogenization temperature increases, so that recrystallized grains did not appear in H350 specimen which was homogenized at the lowest temperature. The fractions of the grain boundary types are also calculated from Fig. 5e-h, plotted and shown in Fig. 5i. The results indicate that as the homogenization temperature decreases from 550 to 490 °C, the fraction of high-angle grain boundaries (HAGBs) has a slight decrease. The grain sizes of both specimens (H550 and H 490) are relatively smaller than the other specimens (H410 and H350), however, a little grain size increase can be seen in H490. Also, by decreasing the homogenization temperature from 490 to 410 °C, the fraction of HAGBs
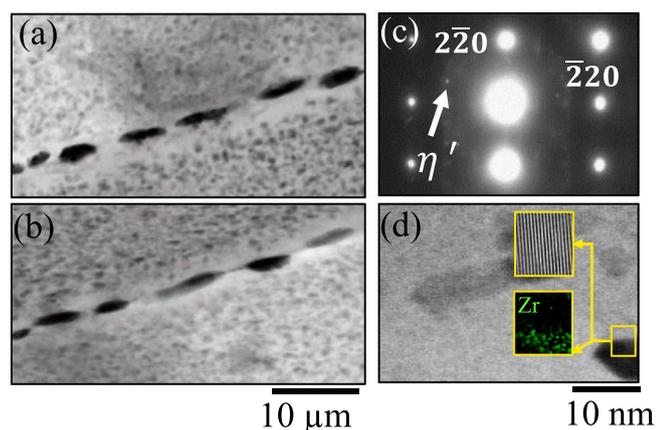
decreased significantly for the specimen in H410 condition, in which an increase in the grain size can be clearly observed. That means the lower recrystallization happens in H410 specimen compared to the H550 and H490 specimens with relatively higher homogenization treatment temperature. By further decreasing the homogenization temperature from 410 to 350 °C, no obvious increase in the fraction of the HAGBs was observed. This result matches the comparable grain sizes of H410 and H350 specimens. The length of low-angle grain boundaries (LAGB) in H350 and H410 specimens is similar and higher than those of H490 and H550 specimens. The LAGBs are known to not be able to trap hydrogen in 7xxx series aluminum alloys [35], meaning that LAGBs do not affect the hydrogen embrittlement of these specimens.

3.2. Hydrogen embrittlement assessment

Fig. 6 shows the nominal stress-strain curves of the specimens obtained by the slow strain rate tensile test (SSRT) technique in dry nitrogen gas (DNG) and humid air (HA) environments. The hydrogen embrittlement sensitivities of the specimens were calculated, and the results are presented in Table 1. From the results in Fig. 6a, it can be found that by increasing the homogenization temperature from 350 to 410 °C, the mechanical properties of the alloy slightly change meaning that the strengths and elongations of H350 and H410 are comparable. Further increasing the homogenization temperature to 490 °C results in the deterioration of both strength and elongation of the alloy. Slight changes in mechanical properties can be observed by further increasing the homogenization temperature from 490 to 550 °C. In H350, H490, and H550 specimens, the total elongations of the specimens were drastically reduced under HA, while the total elongation of H410 specimen decreased slightly. Comparing the values of HE sensitivity indices (I_{HES}) of the specimens shows that HE resistance can be improved considerably by homogenization at 410 °C. Fig. 7a and b show the TEM micrographs of H410 and H490 specimens. The presence of some dislocation loops in Fig. 7a (arrows) shows that Orowan looping is the predominant deformation mechanism in H490 specimen. The formation of these Orowan loops makes the subsequent movement of dislocation more difficult leading to the accumulation of a large number of dislocations in the specimen. While more uniform, finer, and denser Al₃Zr nanoparticles in H410 specimen can be sheared by dislocations leading to a decrease in the dislocation density in the specimen (Fig. 7a). Furthermore, as the homogenization temperature increases, the number and size of dimples decrease. Fig. 7c-h show the fracture surface of the specimens after testing at HA. The fracture surface of H350 specimen exhibited a mixture of transgranular brittle fracture indicated by the quasi-cleavage facet formation in the surface, and the intergranular fracture mode (Fig. 7c). It has been reported [36] that the formation of quasi-cleavage facets is controlled by the initiation of the cracks from precipitates and/or nanoparticles. Shallow dimples were found adjacent to intergranular fracture regions in the fracture surface of the H410 specimen. This observation was consistent with the SSRT results, where the elongation of the H410 specimen was slightly affected by the environment. The fracture surface turned to fully intergranular fracture mode accompanied by some secondary cracks in H490 and H550 specimens (Fig. 7g and h). The secondary cracks were attributable to the H-assisted crack propagation along the grain boundaries [37]. To identify the crack initiation sites in the H350 specimen, a TEM investigation was performed. Fig. 7d shows the cross-section FIB images of TEM lamellae. This cross-section is parallel to the RD-LT plane of the tensile-tested H350 specimen in HA. Fig. 7e shows a TEM image of lamellae containing the crack. The image indicates the formations of voids and secondary cracks in boundaries between the aluminum matrix and Al₃Zr particles in H350 specimen. The corner areas of the fracture surfaces after the tensile testing under DNG are shown in Fig. 8. In all specimens both small and large dimples as an indication of the ductile fracture mode, were observed interspersed on the flat surfaces. In contrast to tensile testing in HA, all specimens show a reasonable trend

Fig. 4. TEM images of the T6 aging state specimens under different homogenization temperature: (a) H410, (b) H490 specimen, (c) an example of the selected area diffraction (SAD) pattern, and (d) Al₃Zr particle and the corresponding IFFT and EDS map of the particle/matrix interface in H410 specimen in T6 aging state.
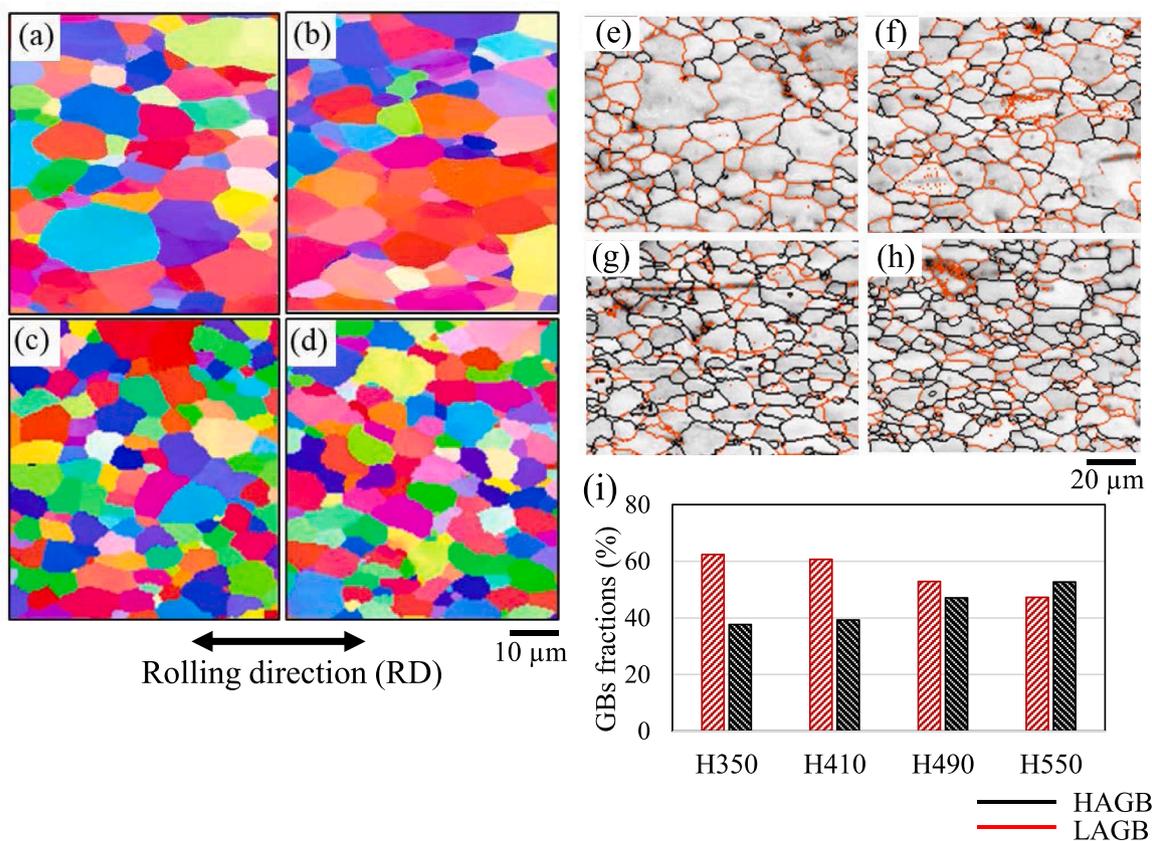
Fig. 5. Inverse pole figure (IPF) micrographs of the specimens with different homogenization temperatures (a) H350, (b) H410, (c) H490, (d) H550; The grain boundaries maps of (e) H350, (f) H410, (g) H490, and (h) H550 specimens, and (i) the grain boundary type fractions.
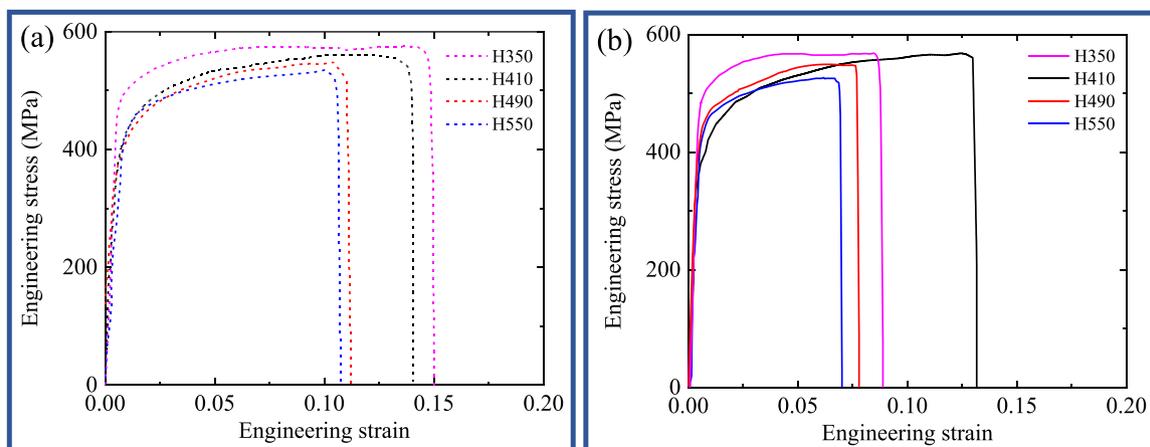

Fig. 6. Slow strain rate testing curves of the specimens in (a) DNG, (b) HA.

Table 1
Mechanical properties and HES indices obtained through slow strain rate test in DNG and HA atmospheres.

Specimen	DNG		HA		I_{HES}
	UTS	el%	UTS	el%	
H550	533	10.7	530	7	0.345
H490	545	11.5	547	7.7	0.33
H410	562	14	566	13.1	0.05
H350	571	15	567	8.8	0.41

in ductility by changing with dispersoid size.

3.3. The hydrogen trapping behavior

Fig. 9a and b show the potential maps obtained from H410 and H490 specimens using scanning kelvin probe force microscopy (SKPFM) after 8 and 120 h measuring times for the same area for each specimen. After 8 h, the matrix and the interiors of nanoparticles have a lower potential than the interface regions in both specimens. The observation of a bright ring around the nanoparticles in SKPFM images implies that the interfacial regions trap more hydrogen than the matrix and interior of nanoparticles. After 120 h, the potential of the matrix and interfacial
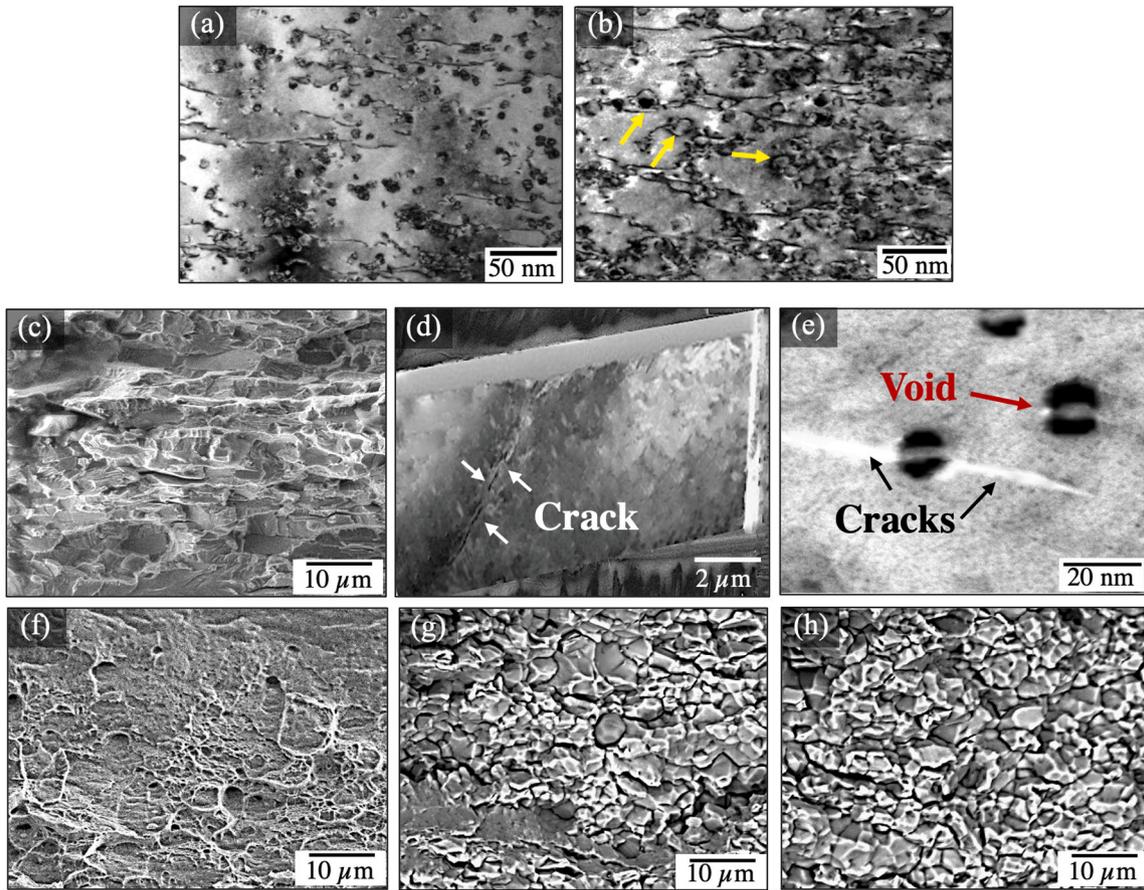
Fig. 7. TEM micrographs showing the particles/dislocation interactions in (a) H410, and (b) H490 specimens. Corner of fracture surface of (c) H350 specimen ruptured in HA, and (d) FIB cross section of the lamella containing microcracks, and (e) Microcracks and voids formed in matrix/ Al₃Zr interfaces in H350 specimen. Corners of fracture surfaces of (f) H410, (g) H490, and (h) H550 specimens ruptured in HA.
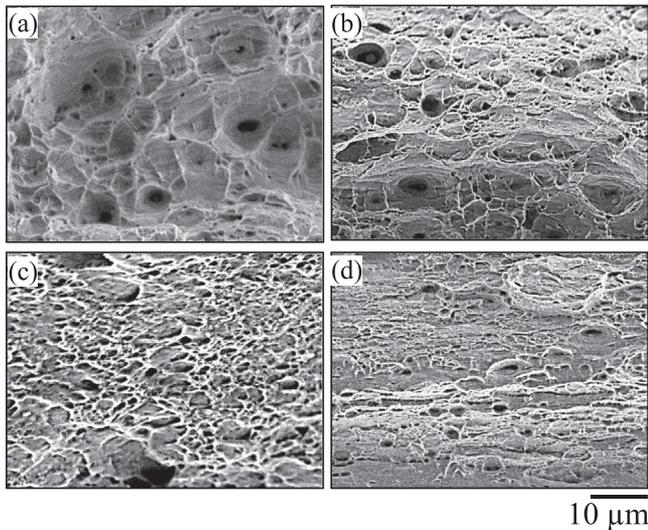

Fig. 8. Corner of fracture surface of (a) H350, (b) H410, (c) H490, and (d) H550 specimens ruptured in DNG.

Fig. 9. SKPFM Observation of (a) H410 and (b) H490 specimens over the time.

regions drastically dropped in the H490 specimen, while, despite a reduction in the potential of the matrix in the H410 specimen, the potential of interfacial regions in this specimen remained high. The presence of dark contrast in the potential maps after 120 h indicates a release of hydrogen from the ma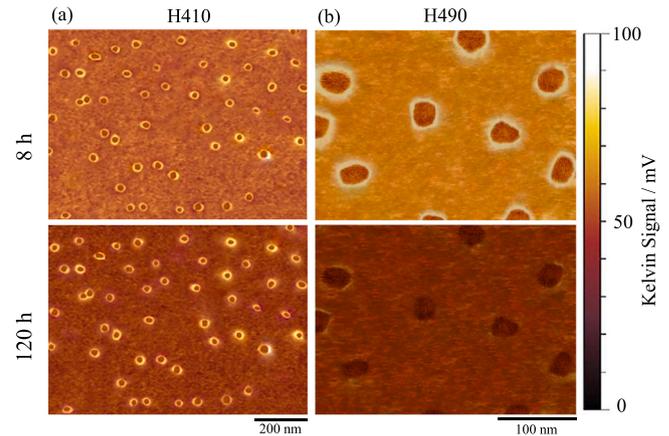trix and interior of nanoparticles in both specimens and also from the interfacial region of the H490 specimen. The hydrogen release from the interfacial regions in H410 was not observed even after 120 h suggesting that the matrix/ nanoparticle interfaces are a strong trap of hydrogen. Furthermore, the potential measured over the matrix in H410 specimen was initially lower than that of H490 specimen. This is most likely due to the irreversible character of the matrix/ nanoparticles interface that can reduce the mobility of hydrogen in the matrix. These results indicate that nanoparticles with different hydrogen trapping abilities can be formed in specimens with different homogenization temperatures.
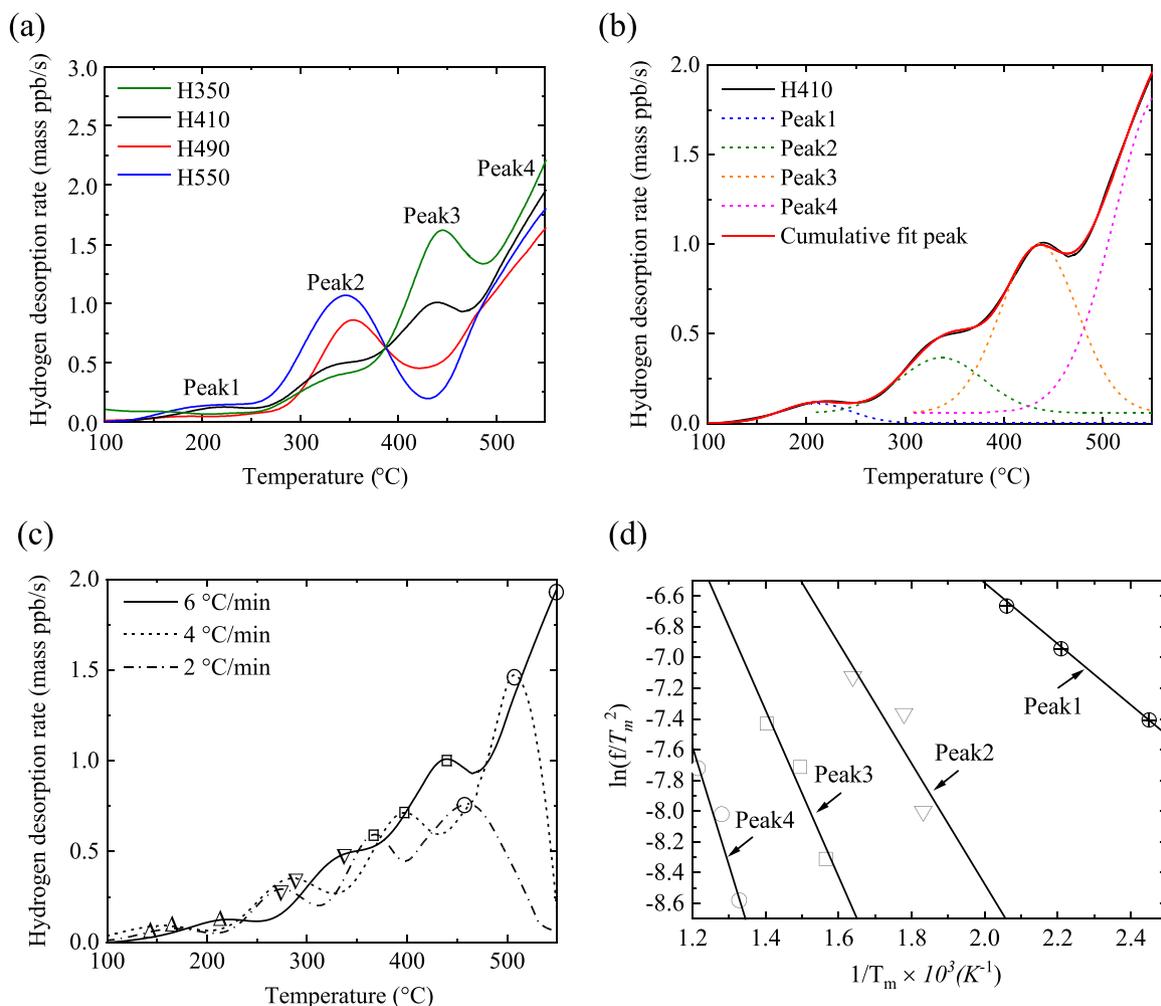
Fig. 10. (a) Effect of the nanoparticle engineering on the thermal desorption spectrum of the studied alloy, (b) deconvolution of the TDS result of H410 specimen into various peaks, (c) the hydrogen desorption spectra of H410 specimen at different heating rates, and (d) the corresponding energy calculation by Choo-Lee method (Eq. (2)).

The rates of the hydrogen desorption of the specimens versus temperature under a constant heating rate of 4 °C/min are presented in Fig. 10a. The TDS results of the specimens were deconvoluted with the Gaussian ideal peak model, as shown in Fig. 10b. The lattice, dislocation, and vacancy traps which are concluded from their excellent agreement with Refs. [18,38] exist in all four specimens. However, H410 and H350 specimens contain another peak (Peak 3) in addition to the mentioned peaks. The SKPFM images showed that the matrix/Al_3Zr nanoparticle interfaces in the H410 specimen are irreversible hydrogen traps. This is in good agreement with the desorption energy of Peak 3, which is 44.95 kJ.mol^{-1} (relatively irreversible). Therefore, it can be deduced that Peak 3 is related to the hydrogen trapped at the Al_3Zr coherent/matrix interfaces. The TDS results also show a higher concentration of hydrogen at the matrix/Al_3Zr coherent interfaces in the H350 specimen than that in the H410 specimen. A detailed explanation of the

reason for thisf phenomenon can be found in the next section. Moreover, the TDS (Table 2) results showed that the dislocations contain the highest and lowest amount of trapped hydrogen in H550 and H350 specimens, respectively. The difference in the amount of hydrogen trapped at dislocation is due to the different dislocation densities of the specimens that resulted from a different dislocation/particle interaction in each specimen (as can be seen in Fig. 7a and b).

4. Discussion

4.1. Engineering of nanoparticles by controlling processing parameters

Ghosh and Ghosh [39] reported that the dissolution of η phase particles (remaining from previous thermal processing like casting) occurs in temperatures more than 475 °C. Thus, during homogenization in

Table 2
Calculated hydrogen binding energies and average concentration of hydrogen of the hydrogen traps.

Peak	Approx. peak position [°C]	Trap site	Desorption energy, E_d [kJ mol^{-1}]	Average concentration of H (mass ppm)			
				H350	H410	H490	H550
1	210	Lattice	16.1	0.053	0.057	0.048	0.061
2	350	Dislocations	32.28	0. 206	0.232	0.356	0.484
3	425	Al_3Zr / matrix interface	44.95	0.741	0.413	-	-
4	> 550	Vacancies	60.40	0.822	0.795	0.776	0.758

lower temperatures namely 350 and 410 °C, a number of η phase particles are still present in the matrix. It is well accepted that the microstructure defects in which surrounding lattice distortion leads to the storage of distortion energy in the matrix, supply preferred nucleation sites for the precipitates [40]. This is due to the fact that the stress field generated by different defects provides the driving force for mass transfer [41]. In the same way, Al₃Zr nanoparticles can precipitate at the interface of a η phase during the homogenization process, since the interface of a η phase provides a fast diffusion path for Zr clusters. The η phase has its highest amount in H350 specimen, meaning that higher heterogeneous nucleation of Al₃Zr nanoparticles can occur in this specimen. The higher nucleation of Al₃Zr nanoparticles in this specimen uses the majority of the Zr content of the matrix leading to a slower growth rate of Al₃Zr nanoparticles. In contrast, the higher homogenization temperature in H490 and H550 specimens can increase the diffusion rate of Zr to produce a coarser and more scattered distribution
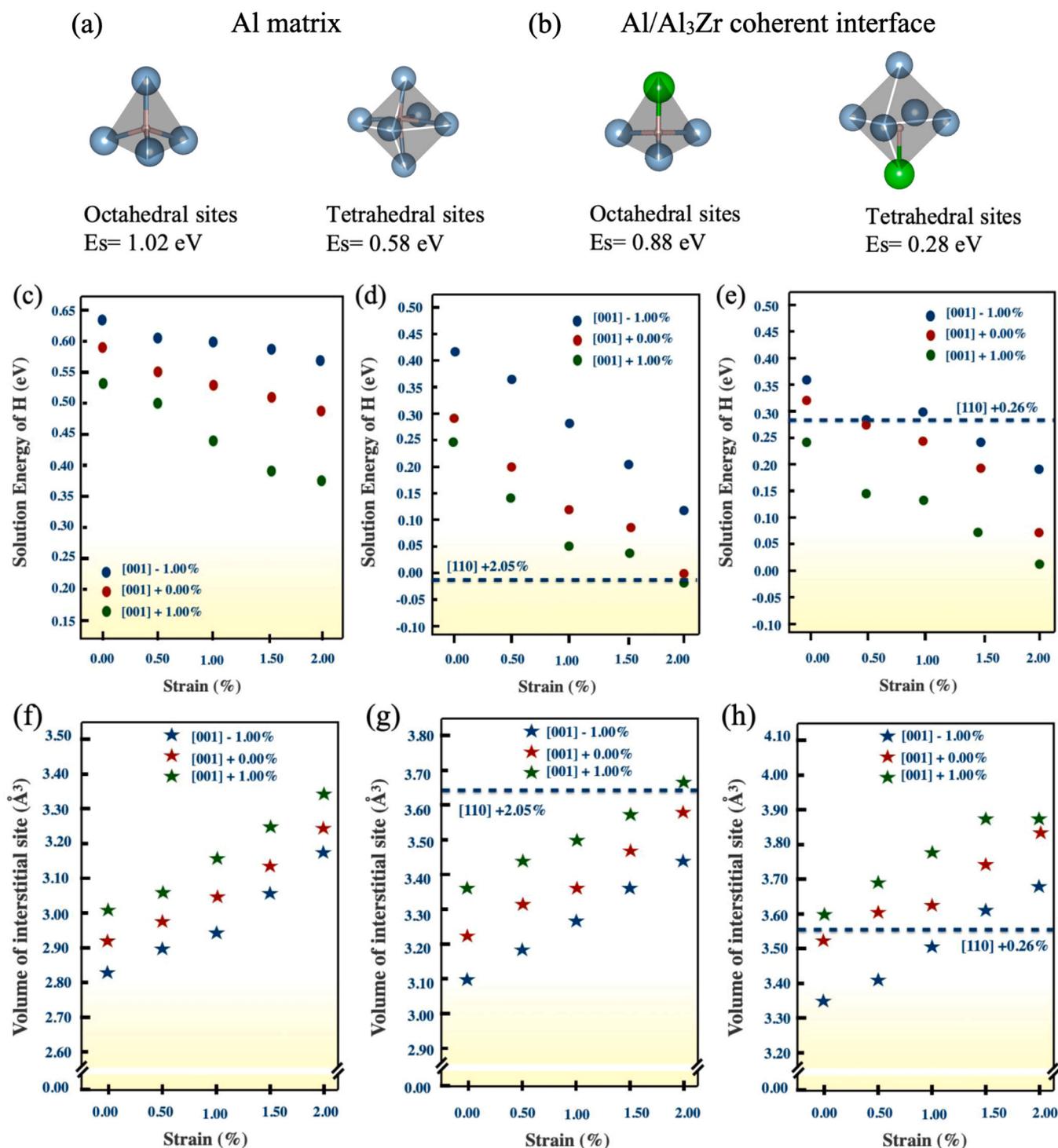
Fig. 11. Theoretical analysis based on DFT simulation: (a,b) The solution energies Es of hydrogen at the octahedral and tetrahedral sites of Al matrix and fully optimized coherent Al/Al3Zr interface that was calculated using DFT, showing the tetrahedral interstitial sites are preferred sites for hydrogen; the computed solution energy as a function of in-plane strain for Al matrix (c), Al/Al₃Zr- L1₂ (d), and Al/Al₃Zr-D0₂₃ (e); and their corresponding volume after the hydrogen trapping at the tetrahedral interstitial site in Al matrix (f), Al/Al₃Zr-L1₂ (g), and Al/Al₃Zr-D0₂₃ (h).

of Al$_3$Zr nanoparticles at the same holding time of homogenization (see Fig. 2c, d).

According to the Zener mechanism [42], the drag force for the migration of grain boundaries is equal to $(\frac{f}{r})$, where f and r are the volume fraction and the average size of the nanoparticles, respectively. Thus, in H350 and H410 specimens the denser distribution of nanoparticles with a finer average size results in a greater $(\frac{f}{r})$, and the higher ability to inhibit recrystallization (as can be seen in Fig. 5a and d). The coarse Al$_3$Zr nanoparticles in H490 and H550 specimens cannot affect properly retarding recrystallization leading to a non-uniform microstructure (Fig. 5c and d).

4.2. Suitability of mechanical responses

The SSRT in DNG showed that lowering the homogenization temperature results in much higher elongations and tensile strengths. The reason for this increase in mechanical properties can be explained by the microstructural changes induced by different homogenization temperatures. Particle shearing and particle bypassing by Orowan looping were observed in the TEM observation of the H410 and H490 specimens, respectively (Fig. 7a, b). When a dislocation shears a coherent Al$_3$Zr nanoparticles the anti-phase boundaries are generated within the sheared nanoparticle [43]. The critical stress required for the generation of the anti-phase boundaries by dislocation gliding is greater than the required stress for bowing a dislocation around the particles. Moreover, particle shearing reduces the dislocation pile-ups (Fig. 7a, b) and thus increases the ductility of the specimens. Therefore, the denser distribution of the fine and coherent Al$_3$Zr nanoparticles in the specimens with the highest homogenization temperatures can enhance the strength and total elongation of the material. Furthermore, uniform, fine and dense Al$_3$Zr nanoparticles result in a more uniform grain size in H350 and H410 specimens by inhibiting the recrystallization. This uniform grain size will significantly increase the elongation and ductility of the specimens [36].

4.3. Key factors for mitigating hydrogen embrittlement

The SKPFM results of the specimens showed that hydrogen accumulation occurs in the matrix/nanoparticles interfaces. To find the most favorable site of a single hydrogen atom in the interface and matrix, the solution energies of all potential sites for hydrogen, including octahedral and tetrahedral sites, were calculated using DFT. The results are summarized in Fig. 11 and Table 3. The solution energies of hydrogen at the tetrahedral sites in the aluminum matrix and Al$_3$Zr/matrix interface were measured to be much lower than octahedral sites suggesting that in agreement with the previous report [44] for pure aluminum, hydrogen tends to occupy the tetrahedral sites rather than octahedral sites. It was known that when the size of nanoparticles is lower than the critical radius for coherency loss, the elastic strain (ε) at the nanoparticle/matrix interface is the largest value and is proportional to $(\frac{a_{dis}-a_{mat}}{a_{mat}})$ where a_{dis} and a_{mat} are the interplanar distances between the

Table 3
H solution energy calculation and H diffusion barrier obtained using DFT calculation. The energy barrier is for hydrogen diffusion from the most stable tetrahedral site to the nearest tetrahedral site for each of the three cases presented in the table.

Interstitial sites (Tetrahedral)	Solution Energy (eV)	Diffusion barrier (eV)
Al	0.58	0.19
Al$_3$Zr/Al Coherent interface	0.28	0.16
Al$_3$Zr/Al Incoherent interface	0.32	0.05
Strained Al$_3$Zr/Al Coherent interface (2.05%)	-0.02	-
Strained Al$_3$Zr/Al Incoherent interface (0.26%)	0.28	-

planes of the nanoparticles and matrix, respectively [16]. Since in L1$_2$-Al$_3$Zr nanoparticle a$_{dis}$ > a$_{mat}$, the nature of the ε is a tensile strain ($\varepsilon > 0$) (see Fig. 2). The increasing of the size of nanoparticles to a size larger than the critical value results in coherency loss by introducing the misfit dislocations (Fig. 2j). The average strain values at the matrix close to the Al$_3$Zr particles for H410 (containing coherent nanoparticles) and H490 (containing semi-coherent nanoparticles) specimens were measured by CalAtom software that were + 2.05% and + 0.26%. The effect of the elastic strain state on hydrogen trapping at the coherent and semi-coherent interfaces was studied using DFT. The hydrogen solution energy corresponding to the tetrahedral sites has a negative value (−0.02 eV) in the coherent interface under the strained condition, while the solution energies corresponding to the tetrahedral sites at the semi-coherent interface under the strained condition and bulk aluminum matrix are 0.28 and 0.58 eV, respectively. This might be because of the increase in the volume of the tetrahedral sites at coherent particle/matrix interface as the result of higher tensile elastic strain compared with the semi-coherent interface and aluminum matrix as can be seen in Fig. 11. These results imply that it is energetically favorable for hydrogen to trap at tetrahedral sites at the coherent interface than those in the bulk aluminum and semi-coherent interface. The diffusion barriers calculated using DFT (Table 3) show a higher diffusion barrier for hydrogen in the fully relaxed coherent interface of Al$_3$Zr /matrix than that for the fully-relaxed interface. This is in good agreement with the results of SKPFM (Fig. 9a, b) showing that hydrogen trapped irreversibly at the coherent interface of Al$_3$Zr/matrix (H410 specimen), while in the semi-coherent interface of Al$_3$Zr/matrix, hydrogen trapped reversibly (H490 specimen). These results showed that high hydrogen diffusion barrier and strong hydrogen trapping at the engineered nanoparticles in H410 specimen provide an excellent aluminum alloy for hydrogen storage applications.

In addition to the influence of the elastic strain on the volume of the tetrahedral sites, the segregation of Zn with a larger atomic radius than Al at the interface of the semi-coherent particles (as shown in Fig. 3b), may contribute to the decrease in volume of tetrahedral sites at this area thereby resulting in the much lower possibility of H trapping by the tetrahedral sites at semi-coherent interface of Al$_3$Zr/matrix. Instead, hydrogen trapping by misfit dislocations most likely will be favored and this is supported by no peak indication in TD spectra of the specimens with the semi-coherent Al$_3$Zr particles (Fig. 10a).

The TDS results (Fig. 10 and Table 2) also revealed that due to the larger number density of Al$_3$Zr particles in H350 specimens and the comparable ε values in H350 and H410 specimens, the amount of trapped hydrogen in Al$_3$Zr/ matrix interface in H350 specimen is significantly higher than that of H410 specimen. This result shows that other factors in addition to ε may affect hydrogen trapping ability at Al$_3$Zr/ matrix interface. The trap site occupancy (θ_T) for Al$_3$Zr/ matrix interfaces in H350 and H410 specimens can be calculated as $\theta_T = \frac{C_T}{N_T}$ [45], where C_T and N_T are trapped hydrogen and trap density, respectively. If it is assumed that the mean distance between Al$_3$Zr particles in H350 and H410 specimens are 20.92 nm and 48.33 nm, respectively, the trap site occupancy of Al$_3$Zr particles in H350 will be 3.80×10^{-17} mass ppm/ particle and in H410 will be 9.66×10^{-17} mass ppm/particle. This shows that despite the higher total hydrogen accumulation in Al$_3$Zr particles in H350 specimen, the number of hydrogen atoms trapped at each Al$_3$Zr particle in H350 specimen is lower than that in H410 specimen. It is reasonable to expect that the misfit elastic area decreases by decreasing the nanoparticle size (as it was indicated in Fig. 12), that most likely leads to less hydrogen trapping and also saturation of trap with a lower amount of hydrogen. Added to this, the fracture surface of H350 specimen is covered mainly with brittle transgranular fracture features which are related to the crack initiation in Al$_3$Zr nanoparticles in the presence of hydrogen (Fig. 7). Given that all parameters except the size of Al$_3$Zr particles are comparable in H350 and H410 specimens, the observation of transgranular fracture mode in H350 can be attributed to
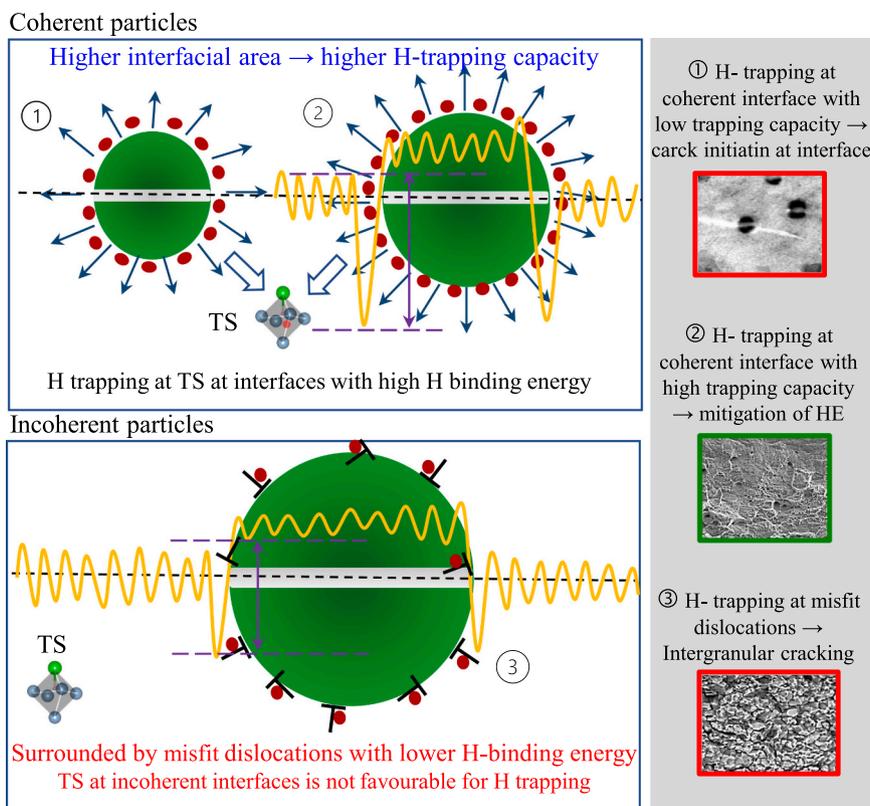
Fig. 12. The schematic depiction of the concept of nano engineering of the particles showing the hydrogen trapping status in different coherent and incoherent interfaces and different hydrogen trapping performances.

the smaller size of Al_3Zr particles. Thus, this can be inferred that in H350 specimen, the Al_3Zr/matrix interfaces reach the critical amount of hydrogen necessary for crack nucleation and then a crack takes place at the interface (as can be seen in Fig. 7). This is because of the fact that the size of nanoparticles can directly affect the number of tetrahedral sites that have relatively low hydrogen solution energy. Therefore, it is concluded that coherent nanoparticles can provide irreversible traps inside the alloys and the size of them influences the HE behavior of the alloy by changing the trap site occupancy and also the critical hydrogen concentration necessary for a crack to nucleate. This agrees with the results reported by Pressouyre [3] indicating that in the external hydrogen situation, some irreversible traps may act as potential flaws and crack initiation sites as the amount of trapped hydrogen reaches quantities higher than the critical hydrogen concentration needed for crack nucleation.

Furthermore, the amount of H trapped at interstitial sites and vacancies is comparable in all specimens while the amount of hydrogen trapped at dislocations increases with an increase in the dislocation density. Hydrogen/dislocation interactions are a very important phenomenon in aluminum alloys. In addition to trapping hydrogen, dislocations can play a dominant role in the hydrogen uptake during plastic deformation in HA [46,47], as well as the distribution of hydrogen [48] inside the specimens. This is due to the relatively low binding energy and reversible nature of the dislocations in aluminum alloys [3,7]. Since dislocations can reversibly trap hydrogen, they cannot be saturated by hydrogen, and thus they cannot operate as crack initiation sites [49]. However, they can work as hydrogen sinks that can locally provide hydrogen to the irreversible traps and crack initiation sites [50].

In specimens with high homogenization temperature, semi-coherent nanoparticles contribute to the higher dislocation density via the Orowan mechanism (Fig. 7) on one hand, and on the other hand, the misfit dislocations are generated in their interface with the matrix, leading to the production of a higher density of hydrogen sources which can

exchange hydrogen with the mobile dislocation, irreversible traps, and grain boundaries. As the hydrogen concentration increases in grain boundaries, the fracture surfaces become flat containing some secondary cracks. In the H550, H490 specimens, the tensile specimen fractures within 6.8% and 7.5% strains, respectively, indicating a large amount of ductility loss due to the presence of hydrogen at the grain boundaries. In these specimens, we supposed that the HE mechanism is mainly the hydrogen-enhanced decohesion (HEDE) mechanism, where the cohesive strength of the grain boundaries is greatly reduced by hydrogen [51–53]. In addition, the change in the fracture mode from ductile dimples to a mixture of dimples with intergranular fracture (Fig. 7) in presence of hydrogen in H410 specimen, indicates that the HEDE mechanism was also active in this specimen. However, irreversibly hydrogen trapping at a high density of homogeneously distributed Al_3Zr nanoparticles in H410 specimen mitigates the repartitioning of hydrogen at intergranular crack tips leading to improving the HE behavior of the specimen.

The nanoparticles in H350 specimen have relatively lower hydrogen occupancy; thus, the interfaces between matrix and nanoparticles can be more easily occupied by hydrogen, and then nano-voids can be formed in these areas leading to the transgranular failure [54]. This failure mechanism is related to the hydrogen-enhanced localized plasticity (HELP) mechanism [55,56] that increases the concentration of the slip bands as can be observed on the fracture surface (Fig. 7). The fracture surface also shows that in addition to HELP mechanism, HEDE is also active, however, the HELP mechanism is dominant (HELP > HEDE), since the fractography of the specimen revealed a dominant transgranular fracture mode.

In the present work, the effect of the size and coherency of the Al_3Zr nanoparticles on their hydrogen-trapping ability, HE sensitivity as well as mechanical properties of the alloy have been studied based on a synergistic experimental-simulation approach. The hydrogen trapping at the semi-coherent interface of the Al_3Zr nanoparticles, which forms

during homogenization in the range of 490–550 °C, is because of the hydrogen residing at the misfit dislocations. These dislocations may act as hydrogen sources inside the alloys leading to the accumulation of the needed hydrogen value at grain boundaries to cause intergranular failure and poor performance in the hydrogen environment. The elastic coherency strain of coherent interfaces increases the volume of the tetrahedral sites and higher diffusion barrier for hydrogen and thus acts as irreversible hydrogen trap sites. The amount of hydrogen that can be trapped by coherent particles depends on the volume of the particles. The smaller Al_3Zr nanoparticles can trap a lower amount of hydrogen due to the lower number of tetrahedral sites. Hence, they can be saturated by hydrogen in lower hydrogen contents, leading to initiation of H-assisted crack at the interface.

5. Conclusion

Using multiscale comprehensive experimental and simulation approaches including Kelvin probe force microscopy, atom probe tomography, thermal desorption spectroscopy, scanning transmission electron microscopy, and density functional theory calculations, we could successfully engineer the nanoparticles in aluminum alloys for the first time to provide ideal material for hydrogen storage applications. The following conclusions can be summarized:

1. Engineering of nanoparticles during production processes is a determinant and important measure for designing aluminum alloys with superior comprehensive properties combining outstanding mechanical properties and excellent resistance to HE.
2. The elastic coherency strain of coherent interfaces of nanoparticles increases the volume of the tetrahedral sites and higher diffusion barrier for hydrogen and thus acts as irreversible hydrogen trap sites with high hydrogen trapping capacity.
3. The smaller Zr nanoparticles can trap a lower amount of hydrogen due to the lower number of tetrahedral sites, leading to easier saturation of hydrogen at tetrahedral sites and thus, crack initiation of the interface.
4. The loss of coherency in the semi-coherent nanoparticles leads to reversibly trapping of hydrogen at misfit dislocations accompanied by a very low diffusion barrier of hydrogen. This increases the hydrogen diffusion and exacerbates the hydrogen embrittlement sensitivity.
5. Depending on the characteristics of particles, e.g. coherency, interface, size, volume and crystal structure of nanoparticles, some are useful to mitigate HE and they are an excellent candidate for use in hydrogen storage applications, some provide hydrogen for vulnerable sites within the alloy, and some act as crack initiation sites.

CRediT authorship contribution statement

Mahdieh Safyari: Conceptualization, Methodology, Funding acquisition, Resources, Visualization, Investigation, Software, Validation, Formal analysis, Supervision, Writing – original draft. **Nabil Khossossi**: Investigation, Software, Supervision, Data curation. **Thomas Meisel**: Methodology, Formal analysis. **Poulumi Dey**: Investigation, Software, Writing – review & editing. **Thomas Prohaska**: Resources, Writing – review & editing. **Masoud Moshtaghi**: Conceptualization, Methodology, Funding acquisition, Resources, Visualization, Investigation, Software, Validation, Formal analysis, Supervision, Writing – review & editing.

Declaration of Competing Interest

The authors declare that they have no known competing financial interests or personal relationships that could have appeared to influence the work reported in this paper.

Data availability

Data will be made available on request.

References

[1] J.R. Scully, G.A. Young, S.W. Smith, 19 - Hydrogen embrittlement of aluminum and aluminum-based alloys, in: R.P. Gangloff, B.P. Somerday (Eds.), Gaseous Hydrogen Embrittlement of Materials in Energy Technologies, Woodhead Publishing, 2012, pp. 707–768, https://doi.org/10.1533/9780857093899.3.707.

[2] W.J. Qi, R.G. Song, X. Qi, H. Li, Z.X. Wang, C. Wang, J.R. Jin, Hydrogen embrittlement susceptibility and hydrogen-induced additive stress of 7050 aluminum alloy under various aging states, J. Mater. Eng. Perform. 24 (2015) 3343–3355, https://doi.org/10.1007/s11665-015-1616-9.

[3] G.M. Pressouyre, Trap theory of hydrogen embrittlement, Acta Metall. 28 (1980) 895–911, https://doi.org/10.1016/0001-6160(80)90106-6.

[4] D.A. Hardwick, M. Taheri, A.W. Thompson, I.M. Bernstein, Hydrogen embrittlement in a 2000-series aluminum alloy, Metall. Trans. A 13 (1982) 235–239, https://doi.org/10.1007/BF02643313.

[5] D. Wang, Z.Y. Ma, Z.M. Gao, Effects of severe cold rolling on tensile properties and stress corrosion cracking of 7050 aluminum alloy, Mater. Chem. Phys. 117 (2009) 228–233, https://doi.org/10.1016/j.matchemphys.2009.05.048.

[6] D. Wang, D.R. Ni, Z.Y. Ma, Effect of pre-strain and two-step aging on microstructure and stress corrosion cracking of 7050 alloy, Mater. Sci. Eng. A 494 (2008) 360–366, https://doi.org/10.1016/j.msea.2008.04.023.

[7] D. Najjar, T. Magnin, T.J. Warner, Influence of critical surface defects and localized competition between anodic dissolution and hydrogen effects during stress corrosion cracking of a 7050 aluminium alloy, Mater. Sci. Eng. A 238 (1997) 293–302, https://doi.org/10.1016/S0921-5093(97)00369-9.

[8] P.A. Rometsch, Y. Zhang, S. Knight, Heat treatment of 7xxx series aluminium alloys—some recent developments, Trans. Nonferrous Met. Soc. China 24 (2014) 2003–2017, https://doi.org/10.1016/S1003-6326(14)63306-9.

[9] M. Ando, M. Senoo, M. Kanno, Environmental embrittlement in air of Al-Zn-Mg-Cu alloys with Cr or Zr, Keikinzoku/J. Jpn. Inst. Light Met. 57 (2007) 19–24.

[10] R.C. Dorward, Relative effects of chromium and zirconium additions to a high-strength Al-Zn-Mg-Cu alloy, Can. Metall. Q. 15 (1976) 243–247, https://doi.org/10.1179/000844376795050660.

[11] H. Zhao, P. Chakraborty, D. Ponge, T. Hickel, B. Sun, C.-H. Wu, B. Gault, D. Raabe, Hydrogen trapping and embrittlement in high-strength Al alloys, Nature 602 (2022) 437–441.

[12] J.D. Robson, P.B. Prangnell, Dispersoid precipitation and process modelling in zirconium containing commercial aluminium alloys, Acta Mater. 49 (2001) 599–613, https://doi.org/10.1016/S1359-6454(00)00351-7.

[13] G. Liu, G.-J. Zhang, X.-D. Ding, J. Sun, K.-H. Chen, Dependence of fracture toughness on multiscale second phase particles in high strength Al alloys, Mater. Sci. Technol. 19 (2003) 887–896, https://doi.org/10.1179/026708303225004314.

[14] P. Wouters, B. Verlinden, H.J. McQueen, E. Aernoudt, L. Delaey, S. Cauwenberg, Effect of homogenization and precipitation treatments on the hot workability of an aluminium alloy AA2024, Mater. Sci. Eng. A 123 (1990) 239–245, https://doi.org/10.1016/0921-5093(90)90289-F.

[15] Clara Escrivà-Cerdán, S.W. Ooi, G.R. Joshi, R. Morana, H.K.D.H. Bhadeshia, Robert Akid, Effect of tempering heat treatment on the CO_2 corrosion resistance of quench-hardened Cr-Mo low-alloy steels for oil and gas applications, Corros. Sci. 154 (2019) 36–48, https://doi.org/10.1016/j.corsci.2019.03.036.

[16] W. Qin, J.A. Szpunar, A general model for hydrogen trapping at the inclusion-matrix interface and its relation to crack initiation, Philos. Mag. 97 (2017) 3296–3316, https://doi.org/10.1080/14786435.2017.1378451.

[17] W. Qin, A. Thomas, Z.Q. Cheng, D. Gu, T.L. Li, W.L. Zhu, J.A. Szpunar, Key factors affecting hydrogen trapping at the inclusions in steels: a combined study using microprint technique and theoretical modeling, Corros. Sci. 200 (2022), 110239, https://doi.org/10.1016/j.corsci.2022.110239.

[18] M. Safyari, M. Moshtaghi, T. Hojo, E. Akiyama, Mechanisms of hydrogen embrittlement in high-strength aluminum alloys containing coherent or incoherent dispersoids, Corros. Sci. 194 (2022), 109895, https://doi.org/10.1016/j.corsci.2021.109895.

[19] S. Abraham, R. Bodnar, J. Raines, Y. Wang, Inclusion engineering and metallurgy of calcium treatment, J. Iron Steel Res. Int. 25 (2018) 133–145, https://doi.org/10.1007/s42243-018-0017-3.

[20] J. Moon, S.-J. Kim, C. Lee, Role of Ca treatment in hydrogen induced cracking of hot rolled API pipeline steel in acid sour media, Met. Mater. Int. 19 (2013) 45–48, https://doi.org/10.1007/s12540-013-1008-3.

[21] S. Yamasaki, H.K.D.H. Bhadeshia, M_4C_3 precipitation in Fe–C–Mo–V steels and relationship to hydrogen trapping, Proc. R. Soc. A 462 (2006) 2315–2330, https://doi.org/10.1098/rspa.2006.1688.

[22] B.A. Szost, R.H. Vegter, P.E.J. Rivera-Díaz-del-Castillo, Hydrogen-trapping mechanisms in nanostructured steels, Metall. Mater. Trans. A 44 (2013) 4542–4550, https://doi.org/10.1007/s11661-013-1795-7.

[23] J. Takahashi, K. Kawakami, Y. Kobayashi, Origin of hydrogen trapping site in vanadium carbide precipitation strengthening steel, Acta Mater. 153 (2018) 193–204, https://doi.org/10.1016/j.actamat.2018.05.003.

[24] J. Yuan, S. Pan, T. Zheng, X. Li, Nanoparticle promoted solution treatment by reducing segregation in AA7034, Mater. Sci. Eng. A 822 (2021), 141691, https://doi.org/10.1016/j.msea.2021.141691.

[25] J.F. Nie, B.C. Muddle, Strengthening of an Al–Cu–Sn alloy by deformation-resistant precipitate plates, Acta Mater. 56 (2008) 3490–3501, https://doi.org/10.1016/j.actamat.2008.03.028.

[26] J. Li, M. Elmadagli, V.Y. Gertsman, J. Lo, A.T. Alpas, FIB and TEM characterization of subsurfaces of an Al–Si alloy (A390) subjected to sliding wear, Mater. Sci. Eng. A 421 (2006) 317–327, https://doi.org/10.1016/j.msea.2006.01.084.

[27] W.Y. Choo, J.Y. Lee, Thermal analysis of trapped hydrogen in pure iron, Metall. Trans. A 13 (1982) 135–140, https://doi.org/10.1007/BF02642424.

[28] G. Kresse, J. Furthmüller, Efficient iterative schemes for ab initio total-energy calculations using a plane-wave basis set, Phys. Rev. B 54 (1996) 11169–11186, https://doi.org/10.1103/PhysRevB.54.11169.

[29] J.P. Perdew, K. Burke, M. Ernzerhof, Generalized gradient approximation made simple, Phys. Rev. Lett. 77 (1996) 3865–3868, https://doi.org/10.1103/PhysRevLett.77.3865.

[30] H.J. Monkhorst, J.D. Pack, Special points for Brillouin-zone integrations, Phys. Rev. B 13 (1976) 5188.

[31] G. Henkelman, B.P. Uberuaga, H. Jónsson, A climbing image nudged elastic band method for finding saddle points and minimum energy paths, J. Chem. Phys. 113 (2000) 9901–9904.

[32] K.E. Knipling, R.A. Karnesky, C.P. Lee, D.C. Dunand, D.N. Seidman, Precipitation evolution in Al–0.1Sc, Al–0.1Zr and Al–0.1Sc–0.1Zr (at%) alloys during isochronal aging, Acta Mater. 58 (2010) 5184–5195, https://doi.org/10.1016/j.actamat.2010.05.054.

[33] S. Malopheyev, V. Kulitskiy, R. Kaibyshev, Deformation structures and strengthening mechanisms in an AlMgScZr alloy, J. Alloy. Compd. 698 (2017) 957–966, https://doi.org/10.1016/j.jallcom.2016.12.289.

[34] B. Forbord, H. Hallem, J. Røyset, K. Marthinsen, Thermal stability of Al3(Scx, Zr1−x)-dispersoids in extruded aluminium alloys, Mater. Sci. Eng. A 475 (2008) 241–248, https://doi.org/10.1016/j.msea.2007.04.054.

[35] M. Moshtaghi, M. Safyari, S. Kuramoto, T. Hojo, Unraveling the effect of dislocations and deformation-induced boundaries on environmental hydrogen embrittlement behavior of a cold-rolled Al–Zn–Mg–Cu alloy, Int. J. Hydrog. Energy 46 (2021) 8285–8299, https://doi.org/10.1016/j.ijhydene.2020.12.028.

[36] K. Wallin, 10.06 – Statistical methods, in: I. Milne, R.O. Ritchie, B. Karihaloo (Eds.), Comprehensive Structural Integrity, Pergamon, Oxford, 2007, pp. 137–157, https://doi.org/10.1016/B978-008043749-1/00328-0.

[37] I.M. Bernstein, A.W. Thompson. Hydrogen Effects in Metals, Metallurgical Society of AIME, Warrendale, PA, 1981, p. 1071.

[38] G.A. Young, J.R. Scully, The diffusion and trapping of hydrogen in high purity aluminum, Acta Mater. 46 (1998) 6337–6349, https://doi.org/10.1016/S1359-6454(98)00343-4.

[39] A. Ghosh, M. Ghosh, Microstructure and texture development of 7075 alloy during homogenisation, Philos. Mag. 98 (2018) 1470–1490, https://doi.org/10.1080/14786435.2018.1439596.

[40] H. Pan, G. Qin, Y. Huang, Y. Ren, X. Sha, X. Han, Z.-Q. Liu, C. Li, X. Wu, H. Chen, C. He, L. Chai, Y. Wang, J. Nie, Development of low-alloyed and rare-earth-free magnesium alloys having ultra-high strength, Acta Mater. 149 (2018) 350–363, https://doi.org/10.1016/j.actamat.2018.03.002.

[41] D. Blavette, E. Cadel, A. Fraczkiewicz, A. Menand, Three-dimensional atomic-scale imaging of impurity segregation to line defects, Science 286 (1999) 2317–2319, https://doi.org/10.1126/science.286.5448.2317.

[42] C. Zener, Grains, phase, and interfaces: an interpretation of microstructure, Trans. Am. Inst. Min. Metall. Soc. 175 (1948), 15–15.

[43] Y. Buranova, V. Kulitskiy, M. Peterlechner, A. Mogucheva, R. Kaibyshev, S. V. Divinski, G. Wilde, Al3(Sc,Zr)-based precipitates in Al–Mg alloy: effect of severe deformation, Acta Mater. 124 (2017) 210–224, https://doi.org/10.1016/j.actamat.2016.10.064.

[44] C. Wolverton, V. Ozoliiṇmmode, M. Asta, Hydrogen in aluminum: first-principles calculations of structure and thermodynamics, Phys. Rev. B 69 (2004), 144109, https://doi.org/10.1103/PhysRevB.69.144109.

[45] M.S. Bhuiyan, H. Toda, Z. Peng, S. Hang, K. Horikawa, K. Uesugi, A. Takeuchi, N. Sakaguchi, Y. Watanabe, Combined microtomography, thermal desorption spectroscopy, X-ray diffraction study of hydrogen trapping behavior in 7XXX aluminum alloys, Mater. Sci. Eng. A 655 (2016) 221–228, https://doi.org/10.1016/j.msea.2015.12.092.

[46] J. Albrecht, I.M. Bernstein, A.W. Thompson, Evidence for dislocation transport of hydrogen in aluminum, Metall. Trans. A 13 (1982) 811–820, https://doi.org/10.1007/BF02642394.

[47] J. Tien, A.W. Thompson, I.M. Bernstein, R.J. Richards, Hydrogen transport by dislocations, Metall. Mater. Trans. A 7 (1976) 821–829, https://doi.org/10.1007/BF02644079.

[48] G. Itoh, T. Jinkoji, M. Kanno, K. Koyama, Effect of impurity hydrogen on the deformation and fracture in an Al-5 mass Pct Mg alloy, Metall. Mater. Trans. A 28 (1997) 2291–2295, https://doi.org/10.1007/s11661-997-0186-3.

[49] M. Dadfarnia, P. Sofronis, T. Neeraj, Hydrogen interaction with multiple traps: can it be used to mitigate embrittlement? Int. J. Hydrog. Energy 36 (2011) 10141–10148, https://doi.org/10.1016/j.ijhydene.2011.05.027.

[50] E. Charitidou, G. Papapolymerou, G.N. Haidemenopoulos, N. Hasiotis, V. Bontozoglou, Characterization of trapped hydrogen in exfoliation corroded aluminium alloy 2024, Scr. Mater. 41 (1999) 1327–1332, https://doi.org/10.1016/S1359-6462(99)00292-4.

[51] H. Luo, W. Lu, X. Fang, D. Ponge, Z. Li, D. Raabe, Beating hydrogen with its own weapon: Nano-twin gradients enhance embrittlement resistance of a high-entropy alloy, Mater. Today 21 (2018) 1003–1009, https://doi.org/10.1016/j.mattod.2018.07.015.

[52] M. Safyari, M. Moshtaghi, S. Kuramoto, Environmental hydrogen embrittlement associated with decohesion and void formation at soluble coarse particles in a cold-rolled Al–Cu based alloy, Mater. Sci. Eng. A 799 (2021), 139850, https://doi.org/10.1016/j.msea.2020.139850.

[53] A. Nagao, M. Dadfarnia, B.P. Somerday, P. Sofronis, R.O. Ritchie, Hydrogen-enhanced-plasticity mediated decohesion for hydrogen-induced intergranular and "quasi-cleavage" fracture of lath martensitic steels, J. Mech. Phys. Solids 112 (2018) 403–430, https://doi.org/10.1016/j.jmps.2017.12.016.

[54] Z. Tarzimoghadam, D. Ponge, J. Klöwer, D. Raabe, Hydrogen-assisted failure in Ni-based superalloy 718 studied under in situ hydrogen charging: the role of localized deformation in crack propagation, Acta Mater. 128 (2017) 365–374, https://doi.org/10.1016/j.actamat.2017.02.059.

[55] H.K. Birnbaum, P. Sofronis, Hydrogen-enhanced localized plasticity—a mechanism for hydrogen-related fracture, Mater. Sci. Eng. A 176 (1994) 191–202, https://doi.org/10.1016/0921-5093(94)90975-X.

[56] M.L. Martin, M. Dadfarnia, A. Nagao, S. Wang, P. Sofronis, Enumeration of the hydrogen-enhanced localized plasticity mechanism for hydrogen embrittlement in structural materials, Acta Mater. 165 (2019) 734–750.